ADVANCED FUNCTIONAL MATERIALS
www.afm-journal.de

Working Principles of Perovskite Photodetectors: Analyzing the Interplay Between Photoconductivity and Voltage-Driven Energy-Level Alignment

Konrad Domanski, Wolfgang Tress, Thomas Moehl,* Michael Saliba, Mohammad Khaja Nazeeruddin, and Michael Grätzel*

Organic–inorganic lead halide perovskites have recently received significant attention as active materials for high-performance photovoltaics and photodetectors. However, the understanding of their operation mechanism remains limited. High-gain, low-voltage $CH_3NH_3PbI_3$ photodetectors in various architectures are demonstrated herein. Photomultiplication in all structures with direct contact of fluorine-doped tin oxide (FTO) and perovskite with the highest responsivity 208 A W^{-1} corresponding to an incident photon-to-current efficiency of 47 000% is observed. Studying the dynamics and temperature dependence, a slow process with an activation energy of 420 ± 90 meV in the time scale of seconds is found, which is essential to photocurrent multiplication. A model based on ion migration to explain the observed transients and the photomultiplication is developed. The accumulation of negative ionic charge at the FTO/perovskite interface under reverse bias lowers the FTO work function allowing for direct hole injection into the perovskite valence band. Under illumination, the conductivity of perovskite is increased and the device behaves similar to a photoconductor.

1. Introduction

Solution-processable organic–inorganic lead halide perovskites with the formula $CH_3NH_3PbX_3$ (where X is Cl, Br, or I) have attracted significant attention as new optoelectronic materials for photovoltaics,[1–8] photodetectors,[9–19] phototransistors,[13,20] light emitting diodes (LEDs),[21] and lasers.[22,23]

The perovskite materials were shown to possess favorable properties for photovoltaic applications,[24] and electrical power conversion efficiencies of 20.1% have been achieved within only five years of development.[25] Recently, it has been demonstrated that organic–inorganic lead halide perovskites are also suitable candidates for high-performance photodetectors.[11,26] Photodetectors, which convert incident optical signals to electrical signals, are key components for optical communication, photography, environmental sensing, medical analysis, astronomy, and safety equipment.[27] An important class of photodetectors are those exhibiting intrinsic photocurrent amplification (gain) meaning that an incident photon triggers an electrical current flow provided by numerous electrons. Gain increases the sensitivity of the detector making it suitable for applications such as receivers in optical fiber communication, high-resolution imaging, single photon counting, and laser microscopy.[28]

Hu et al. demonstrated the first embodiment of a $CH_3NH_3PbI_3$-based photodetector by employing a lateral geometry with a perovskite-filled channel between a pair of conductive contacts.[12,14] This photodetector architecture exhibited gain of several tens under illumination and reverse bias. The authors suggested that a modified Schottky barrier at the gold/perovskite interface gave rise to electron injection resulting in the observed gain.[12] More recently, Lee et al. presented a hybrid perovskite–graphene photodetector employing field effect transistor geometry, which despite the slow dynamics and a nonlinear response, exhibited gain of several hundreds.[13] Adding further to this, Dong et al. introduced a vertical stack geometry device and showed a high gain of ≈500 along with fast response time.[11] The observed photomultiplication was suggested to originate from trapped photogenerated holes inducing band bending, which reduces the Schottky junction thickness at the MoO_3/perovskite interface and allows the electrons to tunnel through the barrier.

While previous work has focused on the performance metrics of perovskite photodetectors, the understanding of their operating principles is still limited. In this work, we present a vertical stack geometry $CH_3NH_3PbI_3$-based photodetector operated at a very low voltage (–0.6 V), which is characterized by a very high average gain of 1300 and a peak incident photon-to-current efficiency (IPCE) of 50 000%. We demonstrate that the

K. Domanski, Dr. W. Tress, Dr. M. Saliba, Prof. M. K. Nazeeruddin
Group for Molecular Engineering of Functional Materials
Institute of Chemical Science and Engineering
École Polytechnique Fédérale de Lausanne
Station 6, CH-1015 Lausanne, Switzerland
E-mail: wolfgang.tress@epfl.ch
K. Domanski, Dr. W. Tress, Dr. T. Moehl, Prof. M. Grätzel
Laboratory of Photonics and Interfaces
Institute of Chemical Science and Engineering
École Polytechnique Fédérale de Lausanne
Station 6, CH-1015 Lausanne, Switzerland
E-mail: thomas.moehl@epfl.ch

DOI: 10.1002/adfm.201503188

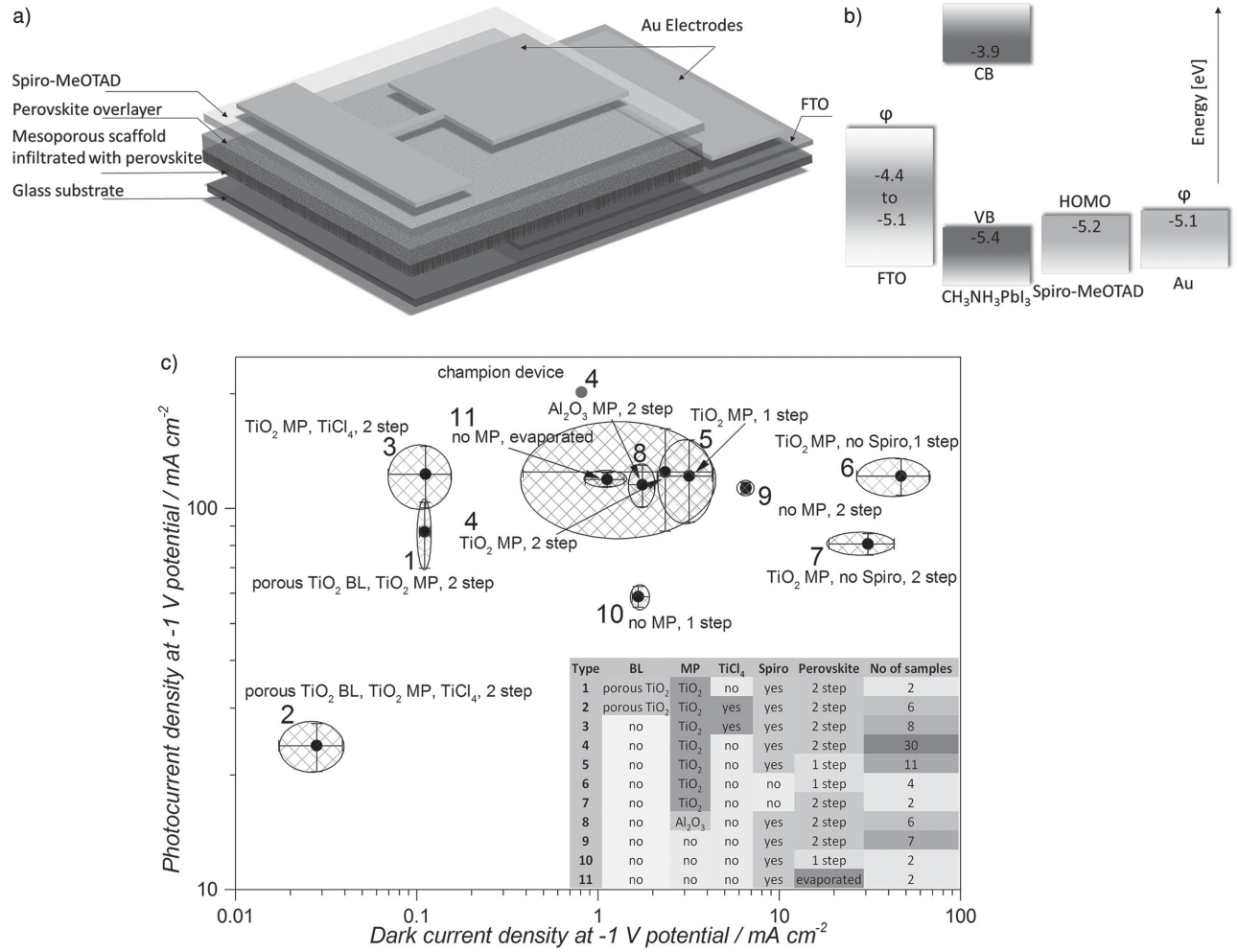

Type	BL	MP	$TiCl_4$	Spiro	Perovskite	No of samples
1	porous TiO_2	TiO_2	no	yes	2 step	2
2	porous TiO_2	TiO_2	yes	yes	2 step	6
3	no	TiO_2	yes	yes	2 step	8
4	no	TiO_2	no	yes	2 step	30
5	no	TiO_2	no	yes	1 step	11
6	no	TiO_2	no	no	1 step	4
7	no	TiO_2	no	no	2 step	2
8	no	Al_2O_3	no	yes	2 step	6
9	no	no	no	yes	2 step	7
10	no	no	no	yes	1 step	2
11	no	no	no	yes	evaporated	2

Figure 1. a) Structure of the model device and b) schematic energy diagram of the hybrid perovskite photodetector.[30] The work function of FTO is not fixed, and it can be changed by interface modification as well as surface treatments.[31] φ: work function, CB: conduction band, VB: valence band, HOMO: highest occupied molecular orbital. c) Dark and photocurrent density under 1 sun illumination as measured under −1 V for devices with different architectures. The ellipses represent standard deviation. Devices with 11 different architectures and an overall more than 100 devices were fabricated. BL: blocking layer; MP: mesoporous scaffold. The data can be found in Table S1 in the Supporting Information.

only prerequisite to obtain high gain in this type of devices is a direct contact between $CH_3NH_3PbI_3$ and fluorine-doped tin oxide (FTO), which shows the versatility of perovskite as a material for high-performance photodetectors.

We investigate steady-state and dynamic behavior of the photodetector with respect to illumination and operating voltage. We find that both, a reduction of the hole injection barrier at the FTO/perovskite interface under reverse bias and an enhancement of conductivity of the perovskite film under illumination (photoconductivity) are essential for the working mechanism. By investigating the temperature dependent dynamics, we find a characteristic activation energy of 420 ± 90 meV for the process dominating the dynamics of the current response. Our findings are consistent with the movement of ionic species alongside electronic charge carriers within perovskite. By assuming that these ions modify the electronic properties of the FTO/perovskite interface, we provide a model for the operation principles of the photodetector.

2. Investigated Architectures

We investigated devices with an architecture similar to our previous design (**Figure 1**a).[26] On top of FTO-patterned glass, a TiO_2 blocking layer (BL) was deposited by spin-coating, spray-pyrolysis or atomic layer deposition (ALD). This was followed by deposition of a mesoporous (MP) metal oxide scaffold (conductive TiO_2 or insulating Al_2O_3). Optionally, $TiCl_4$ treatment was employed at this stage of device fabrication. The $CH_3NH_3PbI_3$ film was deposited using several different methods: interdiffusion of two perovskite precursors (PbI_2 and CH_3NH_3I),[4] orthogonal solvent quenching,[2] or perovskite precursor coevaporation.[29] Finally, the hole transporting material (HTM), Spiro-MeOTAD, was spin-coated and Au contacts were thermally evaporated. Employment of a BL, an MP scaffold, or an HTM was optional and devices in various configurations were studied. A schematic energy diagram of the model devices is shown in Figure 1b. We note that the work function of FTO is not fixed. Depending on the on the surface treatment, or more

precisely, on the surface adsorbates/ dipoles values between –4.4 eV and –5.1 eV are reported. We used a UV–ozone pretreatment of the FTO, which typically results in a work function of –5.1 eV.[31] However, we show later in this report that the work function can be further shifted as a result of ions accumulated at FTO/perovskite interface.

We compared the devices by analyzing their current density–voltage (*J–V*) characteristics. A standard procedure involved measuring dark *J–V* characteristics of the devices from 0 to –1 V (reverse), to +1 V (forward), back to 0 V with 200 mV s^{-1} scan rate. This was followed by an analogous measurement under white, 100 mW cm^{-2} LED illumination. A desirable combination of parameters for the photodetectors was low dark and high photocurrent under reverse bias conditions. We used dark and photocurrent density values at –1 V potential as benchmark parameters to compare fabricated devices and to select the best performers for an in-depth analysis. The summary of our findings is presented in Figure 1c.

The *J–V* studies showed that devices with pinhole-free compact, spray-pyrolyzed, or ALD-deposited TiO_2 BL do not exhibit photocurrent amplification under reverse bias and hence they do not work as photodetectors with gain. We note that already 2 nm thick compact BL deposited on TiO_2 MP completely suppressed photocurrent amplification under reverse bias conditions. Thus, creating an interface between FTO and perovskite proves critical for the photodetector to exhibit gain. We found that replacing a compact BL with a porous one with the same thickness (deposited via spin-coating) introduced photocurrent amplification (gain) under reverse bias conditions. The gain was further increased when the BL was removed completely, which is consistent with an increased FTO/ perovskite contact area. On the other hand, the dark currents also increased when the compact BL was replaced with a porous one and they further increased when the BL was removed completely (**Figure 2**a). Interestingly, dark currents of devices with 2 nm thick ALD-deposited BL were very similar to dark currents of devices employing no BL despite the fact that the former did not show photocurrent amplification. Correspondingly, the shunt resistance (calculated from the slope of the dark current at 0 V) decreased from ≈1 MΩ cm^2 for devices with a compact BL to ≈50 kΩ cm^2 for devices with a porous BL, to ≈10 kΩ cm^2 for devices with ALD or without BL. This indicates that the BL is sufficiently thin for electrons to tunnel through while at the same time a direct contact between FTO and perovskite is prohibited (due to the pinhole-free, conformal BL obtained from ALD even for very thin films). This underlines once again the importance of the FTO/perovskite interface for photocurrent amplification.

The $TiCl_4$ treatment, which creates a 1–3 nm thick porous layer of TiO_2, was found to considerably reduce both dark and photocurrent under reverse bias when applied on samples with a porous TiO_2 BL. However, when applied on devices without a BL and with MP TiO_2, it reduced dark currents while not affecting the photocurrent significantly, which again is in line with the FTO–perovskite interface being responsible for a functioning photodetector.

Furthermore, we compared devices with TiO_2 or Al_2O_3 MP scaffolds. Both scaffolds showed very similar *J–V* characteristics. However, devices without MP scaffold suffered from much increased dark currents (≈8 times increase at –1 V bias) while still showing only slightly lower photocurrents. In order to exclude that the photocurrent amplification phenomena originates from the perovskite/HTM interface, devices without Spiro-MeOTAD layer (and without BL) were fabricated. Such devices still functioned as photodetectors with gain (albeit the gain was much lower than that for devices employing an HTM). However, they suffered from ≈13 times increased dark currents as compared to the devices with an HTM, which can be explained by increased shunting due to a direct contact of MP TiO_2 with gold.

Thus, we conclude that as soon as an intimate contact between FTO and perovskite is present, the device can be operated as a photodetector with gain, regardless of the device architecture or the perovskite deposition method.

We found large variation in photodetector performance of the devices with the same architecture not only between

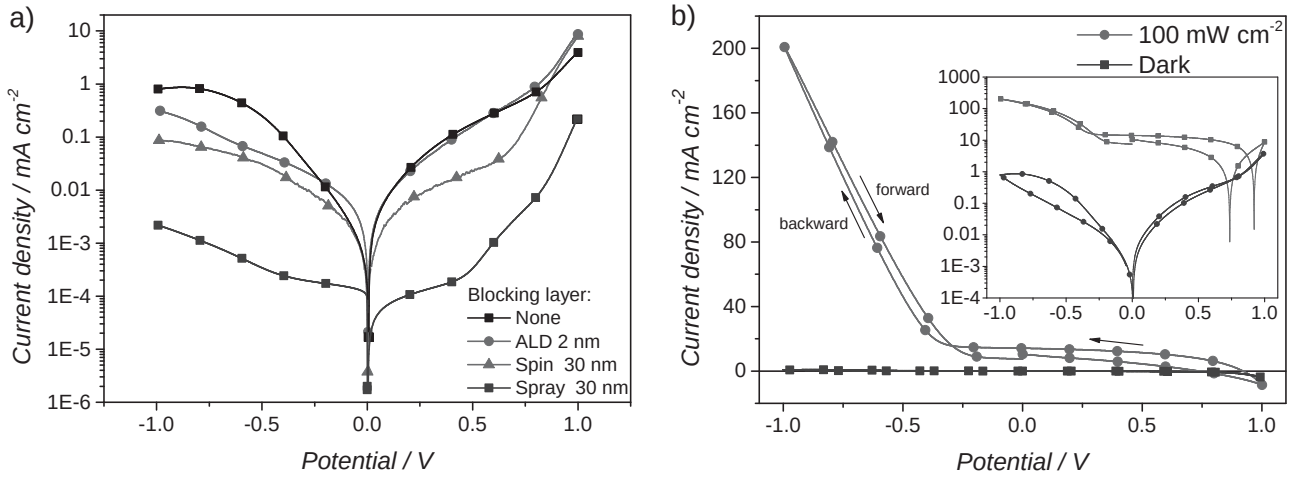

Figure 2. a) Dark *J–V* characteristics of devices with no BL, 2 nm thick ALD compact BL ≈30 nm thick spin-coated porous BL, with ≈30 nm thick spray-pyrolized compact one. b) *J–V* characteristics of a champion device (without a BL) in the dark and under simulated 1 sun illumination. Scan rate: 200 mV s^{-1}.

different batches of devices but also within each batch (the standard error on the photocurrent density at –1 V of 30 model devices was 30%). However, we have not observed any instances of devices without a compact BL, which would not function as photodetectors with gain. Devices employing $CH_3NH_3PbI_3$ can suffer from low reproducibility, which has been a subject of an intense discussion within the photovoltaic community.[32] In general, we observed the highest reproducibility with devices employing no BL and no MP scaffold, although their photodetector performance was limited because of high dark currents from shunting.

Following these findings, we fixed our device architecture for the remainder of this study to a stack of FTO/TiO_2 MP scaffold/$CH_3NH_3PbI_3$/Spiro-MeOTAD HTM/Au (Figure 1a). The $CH_3NH_3PbI_3$ film was deposited via two-step interdiffusion method. We note that this particular architecture yielded the highest-performing devices, however the average performance was not the highest.

3. Device Characterization

3.1. Basic Steady-State Characterization

Measured in the dark, the perovskite photodetector exhibits rectifying behavior. A solar to power conversion efficiency of 6.2% is achieved under 100 mW cm^{-2} simulated solar radiation (Figure 2b). However, when the device under illumination is biased in reverse direction, a strong increase in photocurrent is observed, which allows the device to work as both a photovoltaic cell and a high-gain photodetector depending on the direction of the applied bias.

The spectral response of the detector was characterized under 0 and –0.6 V reverse bias. As shown in **Figure 3**a,b, the detector exhibits high performance across the broad spectrum covering near UV and stretching the entire visible range, while being IR-blind. The IPCE of the device at short circuit conditions falls from ≈60% under 350 nm to ≈30% under 550 nm and ≈20% under 750 nm illumination, which follows the absorbance of the perovskite film (Figure S1, Supporting Information).

Another important parameter for photodetectors is responsivity, which describes the ability of a device to respond to optical signals and it is defined as the ratio of the photogenerated current and the incident light power ($P_{h\nu}$)

$$R = \frac{I_{photo}}{P_{h\nu}} = \frac{I_{illuminated} - I_{dark}}{P_{h\nu}} \quad (1)$$

Under short-circuit conditions the detector is characterized by low responsivity of 0.18–0.11 A W^{-1} in 350–750 nm region.

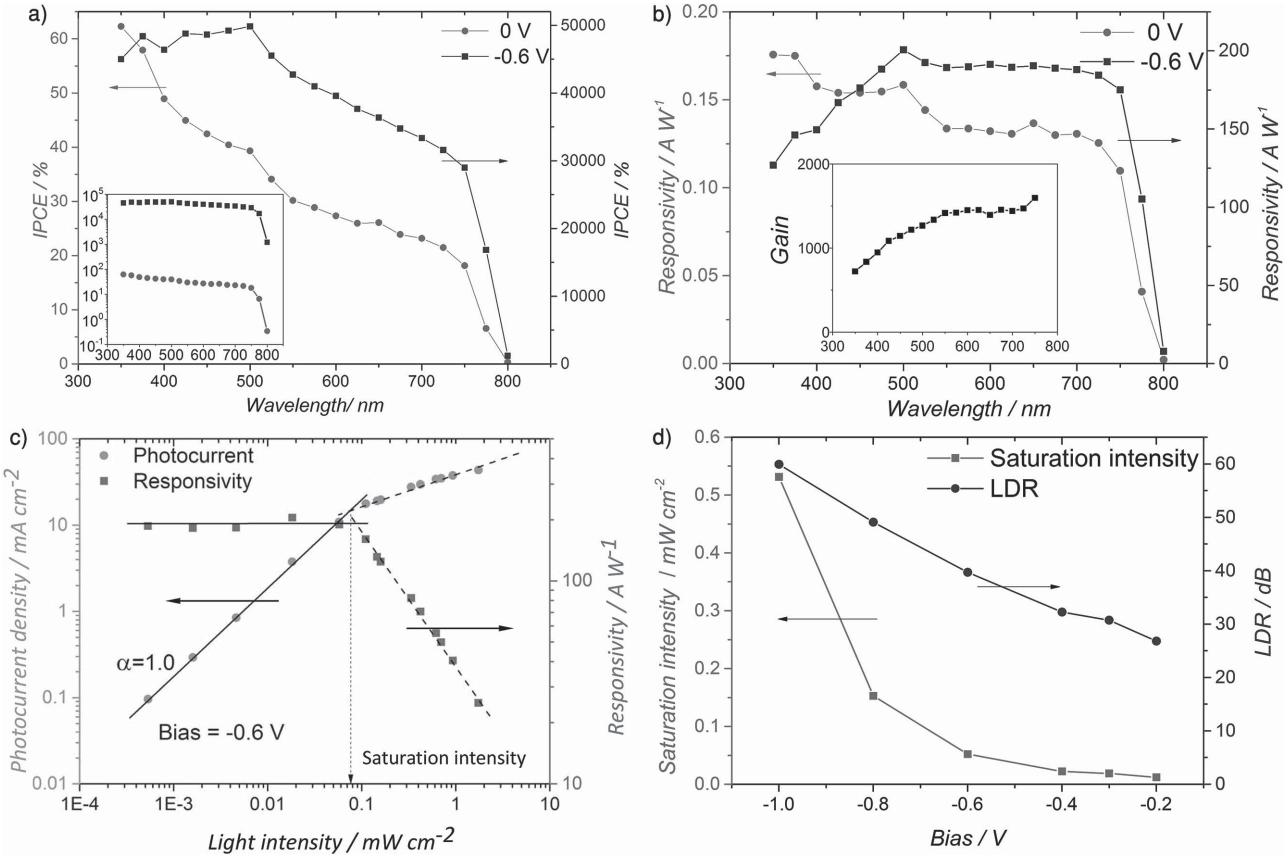

Figure 3. Optoelectronic response of the perovskite photodetector. a) IPCE of the perovskite photodetector (the inset in logarithmic scale), b) responsivity at short-circuit conditions and under –0.6 V reverse bias. The inset shows the gain spectrum of the photodetector. c) Photocurrent and responsivity dependence on light intensity. The lines are fits to a power law. d) Dependence of saturation intensity and LDR on the operating voltage.

To contrast this, when the detector is operated under –0.6 V reverse bias, a peak responsivity up to 200 A W^{-1} and IPCE of 50 000% is observed under 500 nm illumination. The gain spectrum of the detector can be calculated as the ratio of responsivity at –0.6 V bias and at 0 V (short-circuit condition) bias: $\text{gain} = \frac{R_{-0.6V} - R_{sc}}{R_{sc}}$. Gain of 1 indicates that for every pair of photogenerated carriers, there is one additional carrier injected to the perovskite and the overall current flowing through the external circuit is doubled. The gain of the photodetector is found to increase steadily from ≈720 to ≈1600 between 350 nm and 750 nm. This can be attributed to the more homogenous carrier generation within the perovskite layer at longer illumination wavelengths due to a larger penetration depth of the light, which decreases the resistivity of the perovskite more homogeneously.

Linear dynamic range (LDR) describes an illumination intensity range within which the current response of the detector scales linearly with light intensity. It can be obtained as

$$\text{LDR} = 20\log\frac{I_{\text{upper}} - I_{\text{dark}}}{I_{\text{lower}} - I_{\text{dark}}} \quad (2)$$

where I_{upper} is the current value at which the response of the detector deviates from linearity and I_{lower} is the lower resolution limit. For practical applications, it is desirable for a photodetector to have high LDR. However, the device can also be operated outside LDR if its behavior is well characterized.

Below the onset for the photocurrent amplification around –0.2 V, the response of the detector is linear from 0.5 μW cm^{-2} (noise limited) up to at least 100 mW cm^{-2}, which results in LDR of at least 106 dB (Figure S2, Supporting Information). However, when the device is operated under photocurrent amplification conditions, the signal starts to saturate already below the mW cm^{-2} regime (Figure 3c). Photocurrent saturation in photoconductors is known to be related to filling of sensitizing centers.[33] Sensitizing centers are localized states that are empty in the dark and that can capture one type of photogenerated charges, which at low light intensities, increases the overall conductivity of the semiconductor. Under saturation (at higher light intensities), all sensitizing centers are effectively filled. However, the saturation may not be complete either due to the finite lifetime of charges generated above the saturation, or because recombination centers are able to additionally capture some of the photogenerated charges.[33] The saturation intensity of our detector was found to increase substantially under higher operating bias (red line in Figure 3d). Consequently, since the noise limit on the lower end of the linear region (≈0.5 μW cm^{-2}) does not considerably vary with operating voltage, LDR increases when the device is operated under higher reverse bias showing an approximately linear scaling with reverse bias (blue line).

Under –0.6 V reverse bias, we have measured a responsivity of 208 A W^{-1} (IPCE of 47 000%), which is among the highest values reported for perovskite photodetectors.[11,13,19,20] The current response of the device was found to be linear with irradiance up to 80 μW cm^{-2} resulting in a LDR of 44 dB. We note a broad variability for the saturation intensity from 20 to 110 μW cm^{-2} with an average value of 58 μW cm^{-2} measured for six identically fabricated devices under –0.6 reverse bias. The average responsivity of those devices was found as 135 ± 55 A W^{-1}. The high variation in the performance of the detectors is not unusual for optoelectronic devices employing $CH_3NH_3PbI_3$ and it shows that a robust method to fabricate perovskite photodetectors is still subject to ongoing research.

3.2. Transient Light Intensity and Scan-Rate-Dependent Response

The transient photocurrent response of the device was investigated by biasing the device in reverse direction and exposing it to 60 s long pulses of 550 nm monochromatic light. Below the onset for photocurrent amplification (also at J_{sc} and under forward bias), the transient response of the detector is relatively fast (<10 ms) and thus not resolved in the investigated timescale of seconds. When the device is biased beyond the photocurrent amplification onset, i.e. when the device is operated under photocurrent amplification conditions, the dynamics become considerably slower and an initial overshoot in current is observed when the light is switched-on (**Figure 4**a,b). This overshoot becomes less pronounced and it peaks later when the voltage is further increased in reverse direction. Although we have observed this overshoot under any bias past the amplification onset, at higher reverse bias the overshoot may not be distinct enough to be identified easily. Subsequently, when light is switched-off, the current decay is composed of two components—a very fast one (not resolvable on the investigated timescale of 10 ms) and a very slow one (on the order of seconds). The nature of these two components is likely to be fundamentally different and we hypothesize that the slow component arises due to the movement of ionic species in the perovskite.[34,35] This transient behavior is fully reproducible (Figure S3, Supporting Information) and the bandwidth of the detector is determined to be in the sub-Hz region due to the very slow dynamics.

The current decay is slower when the light is switched-off and the devices are operated under higher reverse voltage. The amount of charge flowing through the device, after light is switched-off can be calculated by fitting the decay curves and integrating the area under them. We determine the charge to be in the range of ≈mC cm^{-2} (Figure 4c). This is significantly higher than can be expected from the extraction of trapped photogenerated electronic carriers (the trapped charge carrier density would exceed the atomic density of the material) and it implies a photoinduced long-lived rise in injection current from the contacts, which decays on the timescale of seconds after the light is switched-off. These slow transient phenomena are due to a slow change either of the conductivity of the perovskite or of the charge carrier injection rates at the contacts (or a combination of both), which can be interpreted as a signature of movement of ionic species within the perovskite layer and will be analyzed later in this work.

The photodetector exhibits gain and can be operated as such under any reverse bias greater than the photocurrent amplification onset. However, the responsivity of the device is highly dependent on the operating voltage. Figure 4d shows that below the photocurrent amplification onset at around

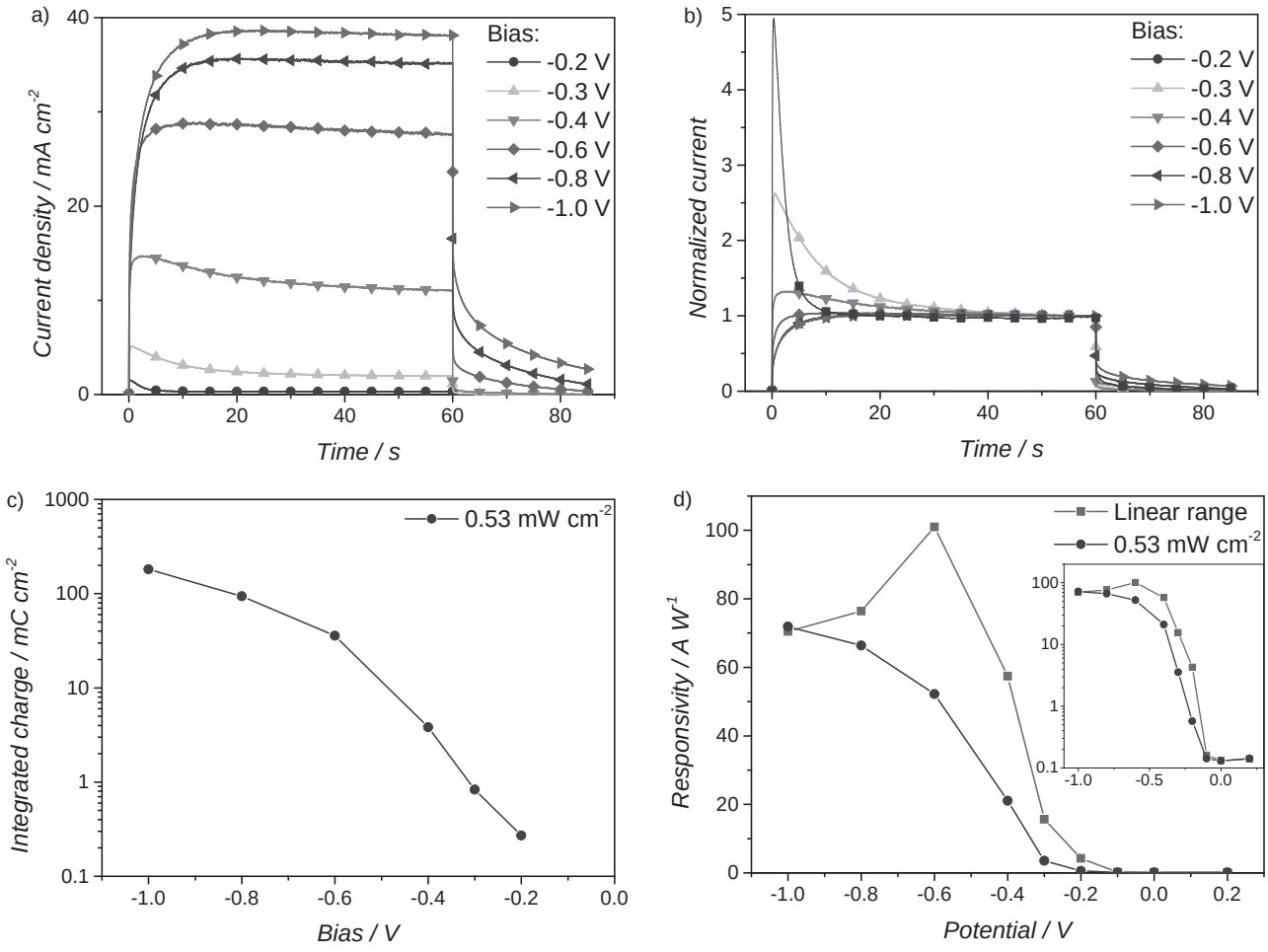

Figure 4. Light-transient response of the perovskite photodetector. a) Transient current response to 60 s long 0.53 mW cm^{-2} pulses of 550 nm light under different reverse bias. The steady-state dark currents are subtracted for each bias; b) transient current response normalized to the steady-state value at 60 s; c) integrated charge flowing after light is switched-off and d) dependence of responsivity on operating bias: under 0.53 mW cm^{-2} illumination and under illumination within LDR the inset in logarithmic scale.

–0.2 V, the responsivity of the device remains very low, which translates to IPCEs below unity. Under higher reverse bias, the responsivity measured within the LDR peaks at –0.6 V before decreasing slightly. The decrease is due to the larger relative contribution of the dark current under higher reverse bias. Under higher illumination intensities (≳0.1 mW cm^{-2}) the decrease is not observed since the relative contribution of the dark current is lower. Interestingly, the responsivity of the device and the total charge flowing through it after light is switched-off follow a very similar trend as a function of operating bias. This may suggest that a photoinduced long-lived rise in injection current is the common origin of both photocurrent amplification and the large amount of post-illumination charge flowing through the device.

The onset of photocurrent amplification at around –0.2 V is found to be independent of light intensity, light spectrum, scan rate, or temperature. However, under reverse bias, past the onset for photocurrent amplification, the slope and the shape of the *J–V* curves are heavily dependent on the illumination intensity (**Figure 5**), scan rate (**Figure 6**), and temperature (**Figure 7**), as will become clear further down.

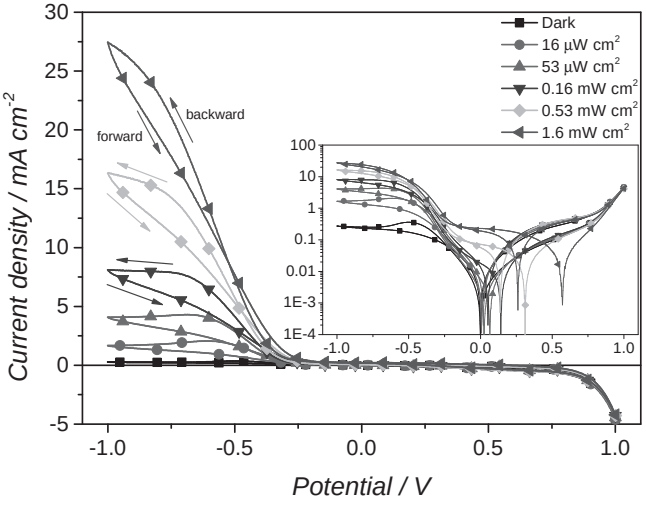

Figure 5. Light intensity dependent *J–V* characteristics of the perovskite photodetector. The inset shows the results in logarithmic scale. Scan rate: 10 mV s^{-1}.

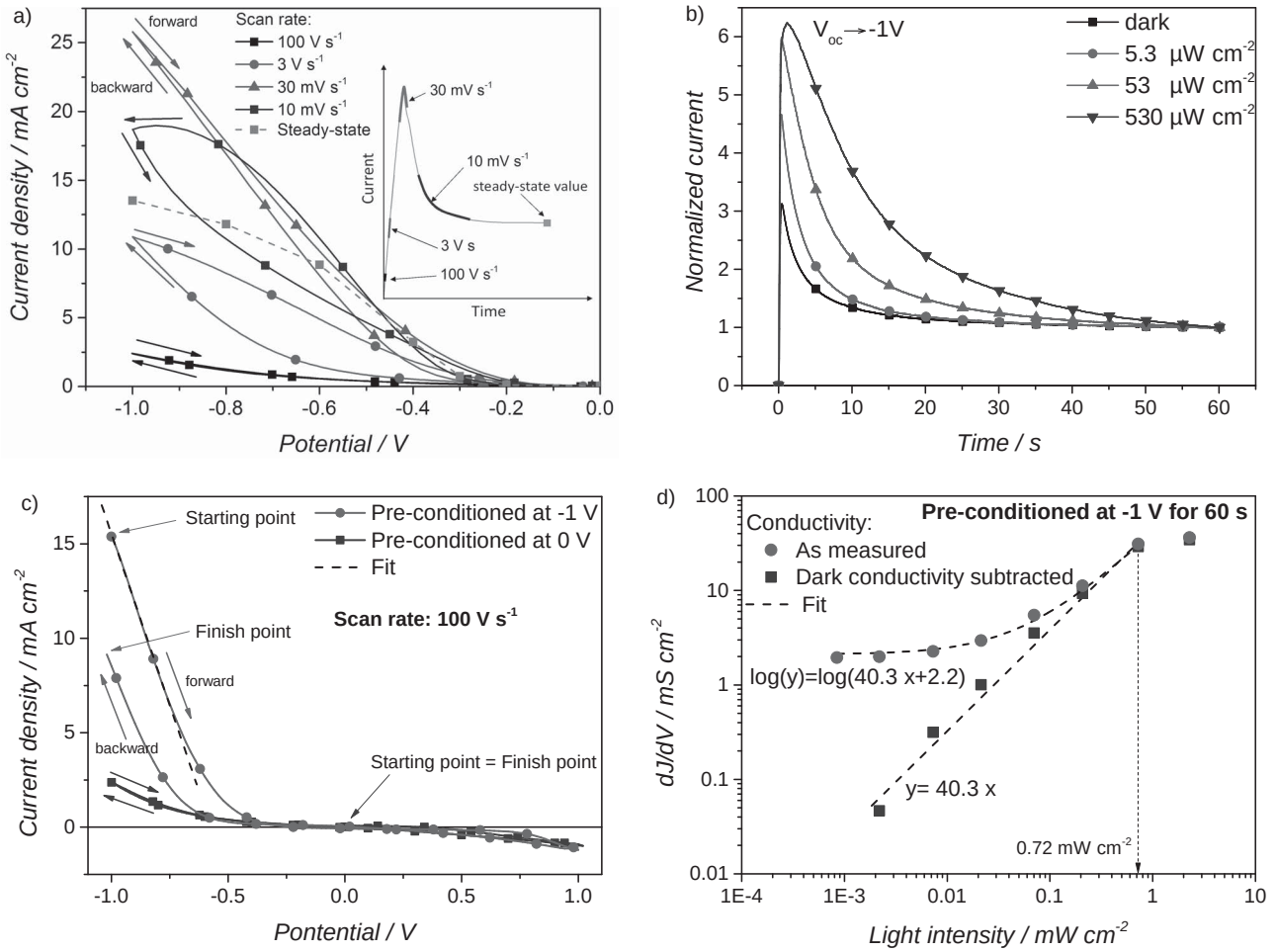

Figure 6. a) The effect of the scan rate on the *J–V* hysteresis of the photodetector (illumination: 550 nm, 530 μW cm^{-2}). The inset shows a schematic voltage transient. b) The response of the device when the potential is step-changed from V_{oc} to –1 V for different light intensities and normalized to the steady-state photocurrent at 60 s. c) *J–V* characteristics of the detector following 60 s of preconditioning at different potentials; illumination: 0.72 mW cm^{-2} for –1 V and 0.53 mW cm^{-2} for 0 V preconditioned data. d*J*/d*V* is found constant between –1 V and –0.6 V in forward scan d) d*J*/d*V* in the linear region as a function of illumination intensity when the detector is preconditioned at –1 V for 60 s. The linearity of conductivity with light intensity indicates photoconductive behavior.

When scanning in backward direction, past the amplification onset, the photocurrent increases sharply with voltage. As the voltage is increased further, the photocurrent saturates and starts to decrease. Scanning beyond this point results in a large *J–V* hysteresis when the scan is then continued in forward direction (cf. curves for intermediate light intensities in Figure 5). In general, the further past the current peak the scan is performed, the larger the hysteresis becomes. The trend was found to hold for all of the devices tested and it is also observed in the dark scans suggesting the independence of the phenomena from light. On the other hand, the point at which the photocurrent starts to saturate is dependent on the illumination intensity. In general, the higher the light intensity, the further the saturation voltage shifts towards reverse bias direction (Figure 5).

The slow photocurrent transients and the hysteresis in the *J–V* curves of Figure 5 anticipate a strong dependence on voltage sweep rate. Thus, we measure the *J–V* curves at different scan rates and following a defined preconditioning point (0 V). Figure 6a shows *J–V* curves measured from 0 V to –1 V and back. When the scan rate is varied, large differences in *J–V* characteristics of the devices are observed. Again, the most pronounced differences are observed when the device is operated under reverse bias. When very high scan rates are employed (order of tens to hundreds V s^{-1}) the photocurrent amplification under reverse bias is almost completely suppressed. Correspondingly, the observed hysteresis is very low. We observe a substantial increase in photocurrent amplification and even higher increase in hysteresis for slightly lower scan rates (several V s^{-1}). The highest photocurrent amplification as well as the lowest hysteresis is obtained when intermediate scan rates are used (30–100 mV s^{-1}). Decreasing the scan rate further to 10 mV s^{-1} results in both lower photocurrent amplification and higher hysteresis. Overlaying these results with steady-state current values (dashed) reveals that even lower scan rates would be required to achieve hysteresis-free curves.

These seemingly anomalous results of the light intensity and scan rate influence on the *J–V* characteristics can

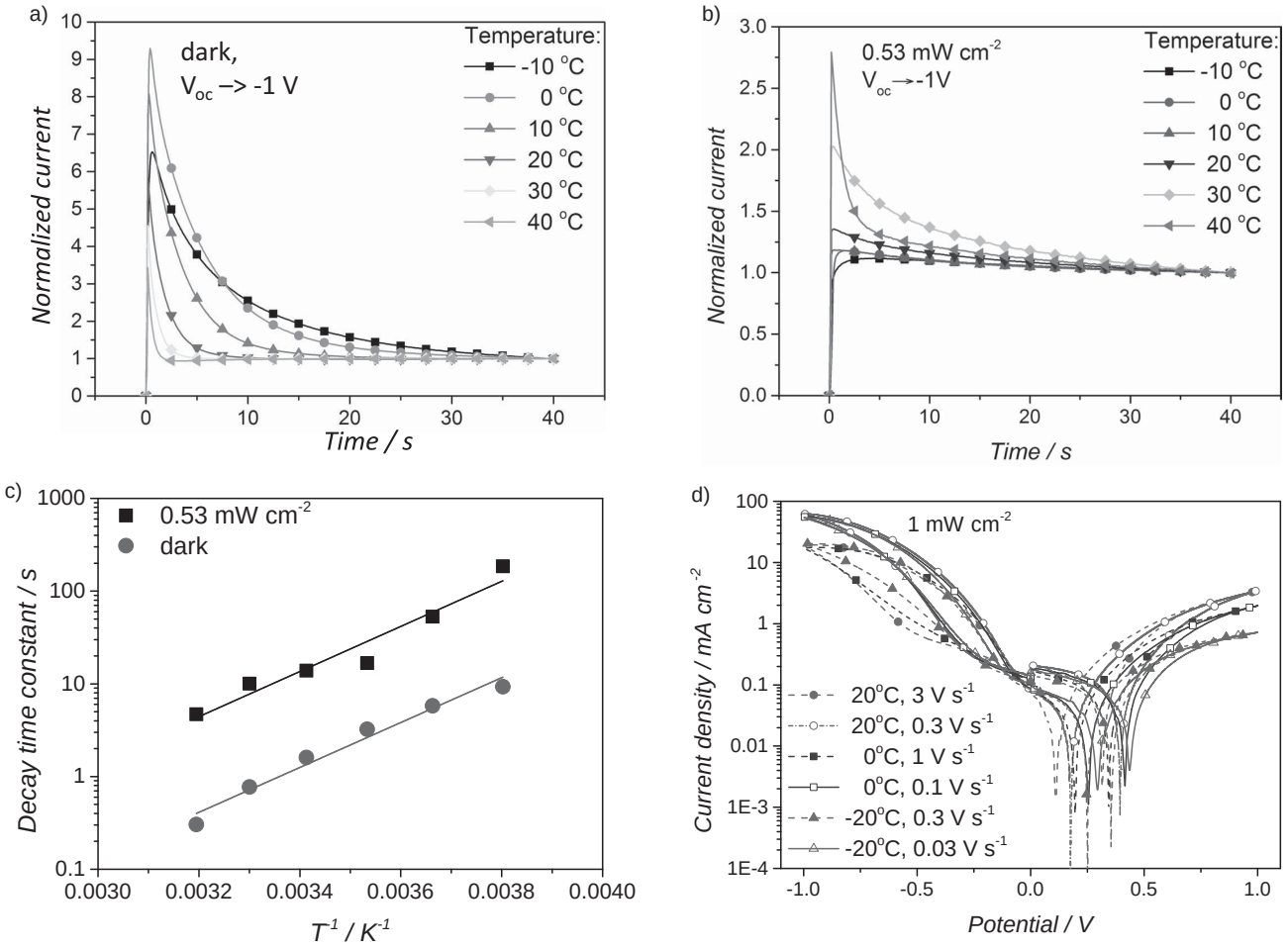

Figure 7. The effect of temperature on the behavior of perovskite photodetector. Transient response of the device when the potential is step-changed from V_{oc} to −1 V at different temperatures normalized to current value at 40 s a) in the dark, b) under 0.53 mW cm^{-2} illumination, and c) the corresponding decay time constants (τ_{decay}) of the transient data fitted to Equation (3). d) Scan rate and temperature dependent *J–V* characteristics of the detector under 1 mW cm^{-2} illumination. Scan rates are selected to visualize the similarity of *J–V* curves measured at an approximately three times lower rate when the temperature was decreased by 20 K.

be explained by investigating the transient behavior of the detector. Figure 6b shows the response of the device when it is subjected to a potential step-change from V_{oc} under corresponding light intensity to −1 V (V_{oc} of the devices was found between 90 mV for 530 µW cm^{-2} and 0 mV in the dark). Interestingly, immediately after the bias is changed to −1 V, almost no current flows through the device neither in the dark nor under light. A relatively slow process is responsible for enabling the current to flow and for photocurrent amplification. However, the same process seems to be responsible for the subsequent overshoot in current, which is followed by a slow decay to a saturation value. The dynamics of this behavior are light intensity dependent and slow down at higher light intensities.

It is possible to model the response of the device to a potential step with two exponential terms, a positive and a negative one

$$J(t) = A_1\left(1 - e^{-t/\tau_{rise}}\right) + A_2 e^{-t/\tau_{decay}} + B \quad (3)$$

The negative term gives rise to the overshoot in current, while the positive term is responsible for the subsequent decay. By fitting the data to this model (Figure S4, Supporting Information) and by analyzing the time constants of the two processes, we have found that light intensity has no apparent influence on the current rise time, which remains below 0.01 s. At the same time, the time constant for current decay decreases from ≈20 s at 1.6 mW cm^{-2} to ≈4 s at 0.53 µW cm^{-2} following closely a power law relationship (Figure S5, Supporting Information). The observed time scale for current decay is comparable to time scales for hysteresis as reported for $CH_3NH_3PbI_3$-based solar cells.[36,37]

The inset in Figure 6a explains how photocurrent amplification and hysteresis are related to the transient behavior presented in Figure 6b. We note that the device does not have sufficient time to establish photocurrent amplification when performing a very fast *J–V* scan. The hysteresis is low since the time interval between forward and reverse scans is very short, which does not permit for significant changes of device's electronic properties; higher current is measured during forward

scan (from –1 V to 0 V). At slower scan rates there is more time to establish photocurrent amplification but consequently the hysteresis increases since the time between backward and forward scans is larger. We "probe the tip" of the transient overshoot by choosing the appropriate scan rate. This way it is possible to achieve nearly hysteresis-free *J–V* curves. When *J–V* scans are performed at a lower rate, the device has sufficient time to reach the "postovershoot" region. Hence the hysteresis becomes higher and now, contrary to the faster measurements, the backward scan yields the higher current value. Based on this, we can explain the shape of the light intensity dependent *J–V* curves presented in Figure 5 under reverse bias and slow scan rates. We have shown that the response of the device to the varying voltage becomes slower when the intensity of the incident illumination is higher. Thus, the hysteresis is lower for larger intensities analogously to the lower hysteresis for intermediate scan rates. This behavior is a consequence of the effect of photogenerated charges on the slow process in the device.

Finally, in Figure 6c, we measured *J–V* characteristics of the device following 60 s of preconditioning at different potentials. Clearly, during a very fast scan, the device cannot respond quickly enough to establish photocurrent amplification. Thus, suppressing the dominance of the slow process for the device response can be achieved by employing a fast 100 V s^{-1} scan rate (40 ms for the complete scan). When the scan is preconditioned at –1 V for 60 s, we observe high photocurrent amplification under reverse bias conditions. Since the contribution of the slow process on the 40 ms timescale is still not negligible, the forward and backward scans do not overlap. Scanning in forward direction, the *J–V* curve is linear between –1 and –0.6 V, which is an indication of photoconductivity as the mechanism responsible for photocurrent amplification. Figure 6d shows how the d*J*/d*V* slope in this linear regime depends on light intensity. The conductivity of the sample is found to be directly proportional to light intensity which is another indication of photoconductivity. However, when plotted in logarithmic scale the relationship is evidently linear only when constant, dark conductivity is subtracted. We note that the response of the detector saturates beyond 0.72 mW cm^{-2} illumination intensity, which is consistent with the value shown in Figure 3 for corresponding operating conditions (0.53 mW cm^{-2}).

3.3. Temperature Dependence

To further analyze the origin of the slow response times, we perform *J–V* and transient measurements as a function of temperature. Figure 7a,b show how the response of the device to a potential step from V_{oc} to –1 V varies at temperatures between –10 and 40 °C (V_{oc} under 0.53 mW cm^{-2} illumination varied with temperature from 150 mV at –10 °C to 50 mV at 40 °C). We investigated the effect of temperature on the dynamics of the device by again fitting the data with the two exponentials model as presented in Equation (3) (Figures S6 and S7, Supporting Information). While the influence of temperature on the current rise time constant was not fully conclusive, we have found that the current decay becomes considerably slower at lower temperatures both in the dark and under illumination (Figure 7c).

Combined analysis of three independent datasets has revealed an Arrhenius-type relationship. Independently of illumination, we derived an activation energy of 420 ± 90 meV for the slow process responsible for the current decay. This value is consistent with the recently reported activation energy for the movement of iodine defects in $CH_3NH_3PbI_3$.[34,35,38]

Subsequently, we observed a strong temperature effect on the *J–V* characteristics of the perovskite photodetector (Figure S8, Supporting Information). In reverse bias direction, photocurrent amplification is found to be heavily dependent both on scan rate and temperature. On the other hand, while the *J–V* characteristics in forward direction are less influenced by the scan rate, the influence of temperature is even more pronounced. The latter is likely due to the reduced conductivity of Spiro-MeOTAD at lower temperatures (Figure S9, Supporting Information). Interestingly, in reverse direction almost identical (rate dependent) *J–V* curves can be obtained when simultaneously changing the scan rate and the temperature (Figure 7d). We have found that decreasing the temperature by 20 K is equivalent to performing the *J–V* scans approximately three times faster (see Figure S8 in the Supporting Information for more examples). This proves once again that the shape of the reverse *J–V* curve describing photocurrent amplification is mainly governed by a temperature-activated slow process. This observation is consistent with the effect of temperature on the transient behavior. Using a first order approximation rate $\propto \exp(-E_a/kT)$, we determine the activation energy to be between 300 and 400 meV, which is remarkably close to the value found above.

In summary, we have found that:

- Direct contact between FTO/perovskite is essential for the device to exhibit photomultiplication.
- Photomultiplication is enabled by slow processes with time constants on the order of seconds established by biasing the device in reverse direction.
- Photomultiplication is a consequence of photoconductivity of $CH_3NH_3PbI_3$. The response of the device becomes slower under illumination.
- The device reacts slower at lower temperatures. Matching *J–V* curves can be obtained by either changing the scan rate or temperature in a controlled way.

4. Results and Discussion

The characteristics of the photodetector are dominated by processes that occur on the time scale of seconds and that are strongly temperature activated. These observations coincide with results from studies on the *J–V* hysteresis in perovskite solar cells. Recently, clear evidence has been presented linking hysteresis with the relatively slow movement of ionic species within the material.[34,35,37,39] Iodine defects (interstitials and vacancies) were shown to have the lowest formation and activation energies for ionic point defects which are suggested to be the mobile species in $CH_3NH_3PbI_3$.[40] Guided by these results, we propose a model explaining the photomultiplication effect in our system.

Figure 8 visualizes how the transient current response to a step-change in potential (from 0 V to negative voltages) arises

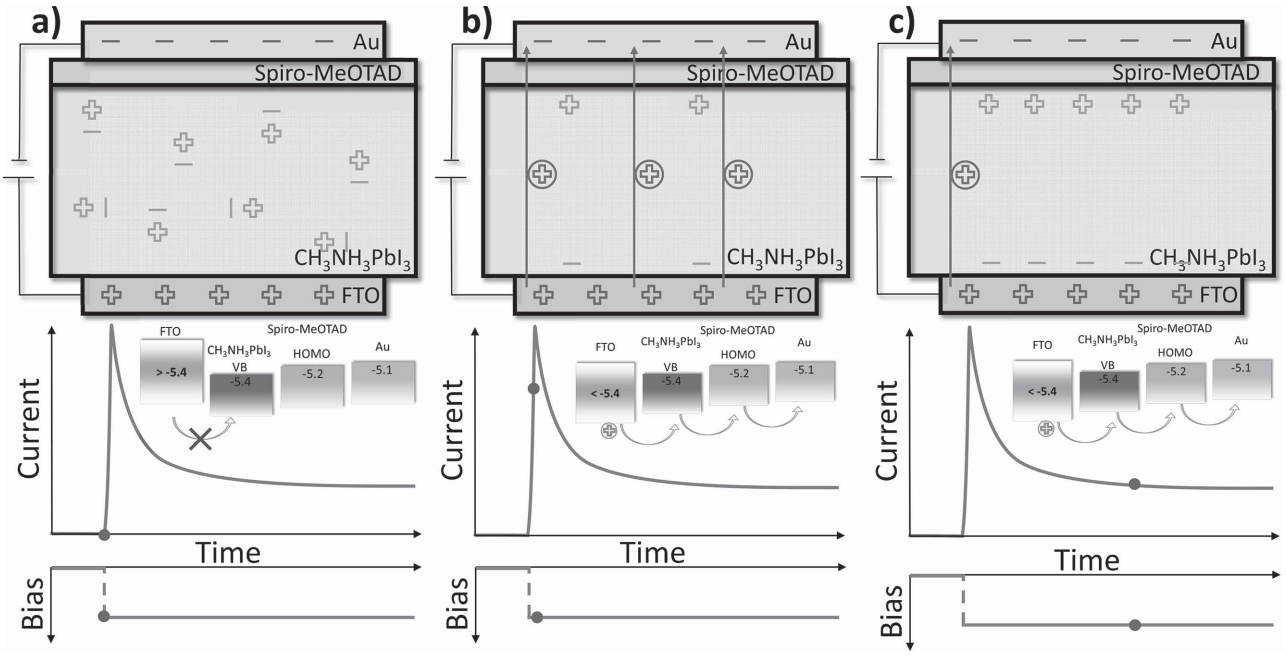

Figure 8. The emergence of transient behavior when the device is kept in dark and it is subjected to a step-change in potential. a) Immediately after applying reverse bias, no current flows through the device since the work function of FTO is too low for hole injection. b) Ions travel to FTO/perovskite interface downshifting FTO work function and enabling hole injection into perovskite. c) As ions accumulate at the interface, they screen the electric field, which results in the decrease of the current. Dark grey charges represent the electric charges on electrodes, light grey mobile ions (in the perovskite), and grey with circle represent the holes injected from FTO. The current–time as well as the distribution of the ions plots are schematic.

due to the movement of mobile ionic species. When the device is kept in the dark, immediately after reverse bias is applied, an (additional) electric field is established across the device but current does not flow due to the unfavorable alignment of FTO work function and $CH_3NH_3PbI_3$ valence band (Figure 8a). Mobile ionic species in $CH_3NH_3PbI_3$ respond to the established electric field and travel towards the respective interfaces where they "pile up." The accumulation of negative ions at $CH_3NH_3PbI_3$/FTO interface causes a downshift of the FTO work function, which enables hole injection into $CH_3NH_3PbI_3$ and results in a flow of dark current across the device (Figure 8b). However, as large amount of ions accumulate at the interfaces, they screen the electric field in the perovskite, which results in the decrease of dark current until equilibrium is reached (Figure 8c).

The effect of temperature on the transient behavior of the detector expresses itself as a modulation in dynamics. We have shown that the time constant of the current decay increases with temperature following an Arrhenius-type relationship (Figure S7, Supporting Information). This is caused by faster diffusion of ionic species at higher temperatures.

Under illumination additional screening effects and interactions of ionic defects with photogenerated charges have to be taken into account. This additional charge can effectively reduce the electric field in the perovskite layer and hence the driving force for ionic species to move; therefore, resulting in slower response times with increased light intensity (Figure 6b). Alternatively, photogenerated charges can compensate the ionic charge accumulated at the interfaces. When the device is kept under constant, reverse bias (past the photocurrent amplification onset) and the light is switched-on, photogenerated charges are attracted to the respective electrodes by the electric field, which is largely screened by the accumulated ions. The transit time of electrons is assumed to be longer than that of holes,[41] which results in fast hole collection and multiple reinjection before the electrons are collected. This way photomultiplication is obtained and thus the device behaves similar to a photoconductor. Additionally, photogenerated charges establish an electric field, which is opposite to the field applied across the device. This induces the diffusion of ions away from the interface, which reduces the screening and results in a slow current increase. Under low reverse operating voltage, a large amount of ions is able to diffuse away from the interface, which in turn results in unfavorable conditions for hole injection.

When the light is switched-off, the relatively low density of ions at the interfaces leads to lower screening and a long-lived rise in injection current from the contacts as compared to the preillumination state (Figure 4c). Essentially, the mechanism responsible for the remnant large injection injection current after light is switched-off is the same as the one shown in Figure 8. The effect is even more pronounced when the device is operated under higher reverse bias, since the electric field remains largely unscreened and hole injection is more efficient.

5. Conclusions

We have fabricated high-gain, low-voltage $CH_3NH_3PbI_3$ photodetectors in various architectures. We observed photomultiplication in all structures having direct contact of FTO and perovskite, i.e. devices with either a porous or without any TiO_2 hole BL. Devices based on FTO/TiO_2 MP scaffold/$CH_3NH_3PbI_3$/Spiro-MeOTAD HTM/Au showed the

highest responsivity of 208 A W^{-1} under 550 nm illumination, which corresponds to an IPCE of 47 000%. These high values of photomultiplication were reached for light intensities in the range of 0.5–80 μW cm^{-2} when the device was biased in reverse (–0.6 V).

During *J–V* scans in the potential range of –1 V and 1 V a strong dependence of the current response on scan rate and preconditioning was observed, showing the highest current values with least hysteresis at moderate scan rate (30 mV s^{-1}). This observation is explained by a slow process in the time scale of seconds found when studying the transient current response upon changing illumination intensity or applied voltage. Having performed temperature dependent studies, we observed a strong dependence of the response time on temperature, yielding an activation energy of 420 ± 90 meV for the slow process. As the values for activation energy and response time are characteristic for ionic motion in these perovskite materials, we develop a model based on ion migration that can explain the observed transients and the photomultiplication. Essential is the pile-up of negative ionic charge at the FTO/perovskite interface under reverse bias. This charge lowers the FTO work function allowing for direct hole injection into the perovskite valence band. Due to an overall increase in conductivity, the hole current is enhanced upon illumination, and the device behaves similar to a photoconductor.

These results on the performance of our photodetector encourage the application of $CH_3NH_3PbI_3$ for low-cost, and highly sensitive photodetectors with high gain. The proposed working principle leads to a better understanding of phenomena such as hysteresis in perovskite-based optoelectronic devices in general and the perovskite interface formation in particular.

6. Experimental Section

Blocking Layer: FTO-patterned glass (Nippon sheet glass, NSG 10 Ω) was cleaned in an ultrasonic bath containing Hellmanex solution for 20 min, and subsequently in isopropanol. This was followed by a UV ozone treatment for 10 min. For devices employing a spin-coated BL, a 0.15 M titanium diisopropoxide bis(acetylacetonate) (TAA) solution (in ethanol) was spin-coated on the FTO at 1000 rpm for 10 s and 2000 rpm for 30 s. This was followed by drying at 125 °C for 5 min and then annealing at 500 °C for 15 min to produce a layer of about 30 nm in thickness. The 30 nm thick TiO_2 compact BL was deposited by spray-pyrolysis of diluted TAA solution (Sigma-Aldrich) at an FTO substrate at 450°C. The solution for spray-pyrolysis was prepared by mixing 1 mL of TAA (30% in 2-propanol) and 25 mL of ethanol. 1–3 nm thick TiO_2 compact BL was deposited by ALD on top of MP TiO_2 scaffolds.

Mesoporous Scaffold: The TiO_2 and Al_2O_3 solutions were prepared by dispersing 1 and 2 g of paste (Dyesol) respectively in 10 mL ethanol and stirring them overnight before use. The solutions were sonicated for 5 min and then spin-coated on the substrates at 2000 rpm for 10 s. The films were dried at 125 °C for 10 s and then annealed at 550 °C for 30 min. This resulted in scaffold thickness of around 100 nm.

$TiCl_4$ Treatment: An optional $TiCl_4$ treatment was performed by immersing the as-prepared scaffolds in a 0.15 M aqueous $TiCl_4$ solution at 70–80 °C for 30 min and then washing them with deionized water and drying. The films were then annealed at 500 °C for 20 min.

$CH_3NH_3PbI_3$ Layer: $CH_3NH_3PbI_3$ films were deposited via several different methods:

Two-step spin-coating: The films were prepared under ambient air atmosphere. 1 M PbI_2 solution was prepared by dissolving 462 mg of PbI_2 (Sigma-Aldrich) in 1 mL *N*,*N*-dimethhylformamide (DMF) under stirring at 70 °C. The hot solution (30 μL) was loaded onto the substrate (10 s loading time) and then spin-coated at 3000 rpm. for 5 s and 6000 rpm for 5 s. Subsequently, the films were transferred to a hotplate at 100 °C for 10 min. After cooling down to room temperature, 200 μL of 0.044 M CH_3NH_3I solution (in isopropanol) was loaded onto the substrate (30 s loading time) and spun at 3000 rpm for 20 s and dried at 100 °C for 5 min.

One-step orthogonal spin-coating: The films were deposited in a nitrogen-filled glove box. A 1.1 M precursor solution of $CH_3NH_3PbI_3$ was prepared by dissolving stoichiometric amounts of PbI_2 and $CH_3NH_3PbI_3$ in dimethylsulfoxide (DMSO). The precursor solution was spin-coated on MP TiO_2 scaffold at 1000 rpm for 10 s, immediately followed by 6000 rpm for 30 s. 10 s before the end of the spin-coating program, chlorobenzene was dropped on the spinning substrate. The substrate was then heated at 90 °C for 1 h.

Evaporation: The evaporation was performed in a vacuum chamber. The perovskite film was coevaporated from PbI_2 and CH_3NH_3I sources through a shadow mask. Both precursors were heating simultaneously to their corresponding sublimation temperatures and the perovskite film was deposited at a substrate placed above the sources.

Hole Transporting Layer and Backside Electrode: A 70×10^{-3} M spiro-MeOTAD solution was prepared by dissolving 72.3 mg of spiro-MeOTAD in 1 mL of chlorobenzene to which 28.8 μL of 4-*tert*-butyl piridine and 17.5 μL of 1.8 M lithium(trifluoromethanesulfonyl)imide (Li-TSFI) solution in acetonitrile were added. The hole transporting layer was prepared by spin-coating the as prepared spiro-MeOTAD solution at 4000 rpm for 30 s. Finally, 80 nm of gold was thermally evaporated through a shadow mask to complete the device.

Device Characterization: The absorption spectrum of the devices was measured using a Hewlett Packard HP 8453 spectrometer. Current–voltage characteristics of the devices were recorded using BioLogic SP200 potentiostat. The source of monochromatic light was a monochromator-filtered xenon lamp. Neutral density filters were used to attenuate the light and a mechanical chopper was used to control the sample illumination. The 100 mW cm^{-2} white light was generated by an array of white LEDs. A heating/cooling sample holder employing a Peltier element was built in order to control the temperature of devices. A thermocouple was used for temperature feedback. The geometry was arranged so that the thermocouple was placed between the Peltier element and the backside of the device. A 0.5 mm thick thermal pad separated the device and the thermocouple.

Supporting Information

Supporting Information is available from the Wiley Online Library or from the author.

Acknowledgements

This work was made possible by the NPRP award [NPRP 6-175-2-070] from the Qatar National Research Fund (a member of The Qatar Foundation). The statements made herein are solely the responsibility of the authors. The authors thank Paul Gratia and Dr. Cristina Roldán Carmona for preparing the evaporated devices, Dr. Juan Pablo Correa for preparing ALD-deposited BL, Agata Mosinska for help with data fitting, and Heidi Francelet for administrative support. W.T. thanks the European Union for funding within the Seventh Framework Program (FP7/2007-2013) under Grant Agreement No. 604032 of the MESO project. T.M. thanks the SNF for financial support through the Nano-tera Synergy project and European Research Council (ERC) for financial support under the Advanced Research Grant (ARG no. 247404) funded under the "Mesolight" project. M.G. thanks the Swiss National Science Foundation for financial support under the Grant No. 200021_157135/1.

Received: July 31, 2015
Revised: August 28, 2015
Published online: October 20, 2015

[1] J. Burschka, N. Pellet, S.-J. Moon, R. Humphry-Baker, P. Gao, M. K. Nazeeruddin, M. Grätzel, *Nature* **2013**, *499*, 316.
[2] N. J. Jeon, J. H. Noh, Y. C. Kim, W. S. Yang, S. Ryu, S. I. Seok, *Nat. Mater.* **2014**, *13*, 897.
[3] A. Kojima, K. Teshima, Y. Shirai, T. Miyasaka, *J. Am. Chem. Soc.* **2009**, *131*, 6050.
[4] J.-H. Im, I.-H. Jang, N. Pellet, M. Grätzel, N.-G. Park, *Nat. Nano.* **2014**, *9*, 927.
[5] N. J. Jeon, J. H. Noh, W. S. Yang, Y. C. Kim, S. Ryu, J. Seo, S. I. Seok, *Nature* **2015**, *517*, 476.
[6] K. Wojciechowski, M. Saliba, T. Leijtens, A. Abate, H. J. Snaith, *Energ. Environ. Sci.* **2014**, *7*, 1142.
[7] O. Malinkiewicz, A. Yella, Y. H. Lee, G. M. Espallargas, M. Graetzel, M. K. Nazeeruddin, H. J. Bolink, *Nat. Photo.* **2014**, *8*, 128.
[8] D. Liu, T. L. Kelly, *Nat. Photo.* **2014**, *8*, 133.
[9] Y. Guo, C. Liu, H. Tanaka, E. Nakamura, *J. Phys. Chem. Lett.* **2015**, *5*, 1748
[10] D. Li, G. F. Dong, W. Z. Li, L. D. Wang, *Sci. Rep.* **2015**, *5*, 7902.
[11] R. Dong, Y. Fang, J. Chae, J. Dai, Z. Xiao, Q. Dong, Y. Yuan, A. Centrone, X. C. Zeng, J. Huang, *Adv. Mater.* **2015**, *27*, 1912.
[12] X. Hu, X. D. Zhang, L. Liang, J. Bao, S. Li, W. L. Yang, Y. Xie, *Adv. Funct. Mater.* **2014**, *24*, 7373.
[13] Y. Lee, J. Kwon, E. Hwang, C. H. Ra, W. J. Yoo, J. H. Ahn, J. H. Park, J. H. Cho, *Adv. Mater.* **2015**, *27*, 41.
[14] H.-R. Xia, J. Li, W.-T. Sun, L.-M. Peng, *Chem. Commun.* **2014**, *50*, 13695.
[15] Q. Lin, A. Armin, D. M. Lyons, P. L. Burn, P. Meredith, *Adv. Mater.* **2015**, *27*, 1969.
[16] Y. Fang, J. Huang, *Adv. Mater.* **2015**, *27*, 2804.
[17] S. Zhuo, J. Zhang, Y. Shi, Y. Huang, B. Zhang, *Angew. Chem. Int. Ed.* **2015**, *127*, 5785.
[18] L. Dou, Y. Yang, J. You, Z. Hong, W.-H. Chang, G. Li, Y. Yang, *Nat. Commun.* **2014**, *5*, 5404.
[19] H.-W. Chen, N. Sakai, A. K. Jena, Y. Sanehira, M. Ikegami, K.-C. Ho, T. Miyasaka, *J. Phys. Chem. Lett.* **2015**, *6*, 2622.
[20] F. Li, C. Ma, H. Wang, W. Hu, W. Yu, A. D. Sheikh, T. Wu, *Nat. Comun.* **2015**, *6*, 8238.
[21] Z.-K. Tan, R. S. Moghaddam, M. L. Lai, P. Docampo, R. Higler, F. Deschler, M. Price, A. Sadhanala, L. M. Pazos, D. Credgington, F. Hanusch, T. Bein, H. J. Snaith, R. H. Friend, *Nat. Nano.* **2014**, *9*, 687.
[22] F. Deschler, M. Price, S. Pathak, L. E. Klintberg, D.-D. Jarausch, R. Higler, S. Hüttner, T. Leijtens, S. D. Stranks, H. J. Snaith, M. Atatüre, R. T. Phillips, R. H. Friend, *J. Phys. Chem. Lett.* **2014**, *5*, 1421.
[23] G. Xing, N. Mathews, S. S. Lim, N. Yantara, X. Liu, D. Sabba, M. Grätzel, S. Mhaisalkar, T. C. Sum, *Nat. Mater.* **2014**, *13*, 476.
[24] G. Xing, N. Mathews, S. Sun, S. S. Lim, Y. M. Lam, M. Grätzel, S. Mhaisalkar, T. C. Sum, *Science* **2013**, *342*, 344.
[25] W. S. Yang, J. H. Noh, N. J. Jeon, Y. C. Kim, S. Ryu, J. Seo, S. I. Seok, *Science* **2015**, *348*, 1234.
[26] T. Moehl, J. H. Im, Y. H. Lee, K. Domanski, F. Giordano, S. M. Zakeeruddin, M. I. Dar, L.-P. Heiniger, M. K. Nazeeruddin, N.-G. Park, *J. Phys. Chem. Lett.* **2014**, *5*, 3931.
[27] S. Donati, *Photodetectors: Devices, Circuits, and Applications*, Prentice-Hall PTR, Upper Saddle River, NJ, USA **2000**.
[28] R. McIntyre, *Measurement* **1985**, *3*, 146.
[29] M. Liu, M. B. Johnston, H. J. Snaith, *Nature* **2013**, *501*, 395.
[30] H.-S. Kim, C.-R. Lee, J.-H. Im, K.-B. Lee, T. Moehl, A. Marchioro, S.-J. Moon, R. Humphry-Baker, J.-H. Yum, J. E. Moser, *Sci. Rep.* **2012**, *2*, 591.
[31] M. Helander, M. Greiner, Z. Wang, W. Tang, Z. Lu, *J. Vac. Sci. Technol. A* **2011**, *29*, 011019.
[32] D. A. Egger, E. Edri, D. Cahen, G. Hodes, *J. Phys. Chem. Lett.* **2015**, *6*, 279.
[33] R. H. Bube, C. T. Ho, *J. Appl. Phys.* **1966**, *37*, 4132.
[34] T. Y. Yang, G. Gregori, N. Pellet, M. Grätzel, J. Maier, *Angew. Chem. Int. Ed.* **2015**, *127*, 8016.
[35] E. T. Hoke, D. J. Slotcavage, E. R. Dohner, A. R. Bowring, H. I. Karunadasa, M. D. McGehee, *Chem. Sci.* **2015**, *6*, 613.
[36] E. Unger, E. Hoke, C. Bailie, W. Nguyen, A. Bowring, T. Heumüller, M. Christoforo, M. McGehee, *Energ. Environ. Sci.* **2014**, *7*, 3690.
[37] W. Tress, N. Marinova, T. Moehl, S. Zakeeruddin, M. K. Nazeeruddin, M. Grätzel, *Energ. Environ. Sci.* **2015**, *8*, 995.
[38] Y. Yuan, J. Chae, Y. Shao, Q. Wang, Z. Xiao, A. Centrone, J. Huang, *Adv. Energy Mater.* **2015**, *27*, 1912.
[39] Z. Xiao, Y. Yuan, Y. Shao, Q. Wang, Q. Dong, C. Bi, P. Sharma, A. Gruverman, J. Huang, *Nat. Mater.* **2015**, *14*, 193.
[40] J. M. Azpiroz, E. Mosconi, J. Bisquert, F. De Angelis, *Energ. Environ. Sci.* **2015**, *8*, 2118.
[41] Q. Dong, Y. Fang, Y. Shao, P. Mulligan, J. Qiu, L. Cao, J. Huang, *Science* **2015**, *347*, 967.